

Role of Oxygen during Methane Oxidation on Pd₁/PdO₁@CeO₂ Surface: A Combined Density Functional Theory, Microkinetic, and Machine Learning Approach

Shalini Tomar,[†] Hojin Jeong,[‡] Joon Hwan Choi,[‡] Seung-Cheol Lee,^{†,¶} and Satadeep Bhattacharjee^{*,†}

[†]*Indo-Korea Science and Technology Center (IKST), Bangalore, India*

[‡]*Korea Institute of Materials Science (KIMS), South Korea*

[¶]*Electronic Materials Research Center, Korea Institute of Science & Technology, Korea*

E-mail: jchoi@kims.re.kr, leesc@kist.re.kr, s.bhattacharjee@ikst.res.in

Abstract

This work explores the role of oxygen in the industrial-based methane oxidation process for its catalytic decomposition. Oxygen, as a well-known oxidizing agent, plays a pivotal role in methane oxidation by facilitating the conversion of methane (CH₄) into carbon dioxide (CO₂) and water (H₂O). We report, how oxygen influences methane oxidation on single Pd and PdO clusters supported on the CeO₂(111) surface. Oxygen is introduced through two distinct mechanisms: (1) directly as part of palladium oxide (PdO), and (2) indirectly through the interaction of oxygen with a single Pd atom, which forms PdO_x clusters on the CeO₂(111) surface. Through DFT calculations, we explored several reaction pathways of methane oxidation on the Pd₁/PdO₁@CeO₂(111) surface, and both Pd & PdO single clusters were found to thermodynamically favor

this process. The DFT calculated activation barrier for methane activation is 0.63 eV on PdO₁@CeO₂(111). Notably, our results also highlight the crucial role of a single Pd atom in oxygen dissociation, which facilitates the formation of PdO₂ species. The presence of oxygen significantly lowers the activation barrier for methane oxidation by 0.36 eV, thereby improving the catalytic efficiency compared to oxygen-deficient conditions. We further explored the reaction selectivity, coverage-dependent production rates, degree of rate control, and turnover frequency using microkinetic modeling. The analysis reveals that the conversion of CH₄ into CO₂ and H₂O predominantly occurs at high temperatures. The rate constants for various reaction steps were derived using the Sure Independence Screening and Sparsifying Operator (SISSO) method, a machine learning-based symbolic regression approach. This allowed us to build a predictive model for the rate constants, leveraging descriptors such as charge, coordination number, and interatomic distances, providing deeper insight into the factors influencing catalytic activity. These findings offer valuable guidance for optimizing catalysts for methane oxidation, a reaction of significant environmental and industrial importance.

Introduction

Methane (CH₄) is a significantly more potent greenhouse gas than carbon dioxide (CO₂)^{1,2} and to reduce the methane emission, catalytic decomposition of unburned CH₄ is essential.^{3–5} The conversion of methane is challenging due to its substantial energy barrier, which arises from the molecule's high symmetry and the strong interactions of its C–H bonds.^{6–8} A widely recognized approach for methane decomposition is by using oxygen, a well-known oxidizing agent, which facilitates the conversion of methane into CO₂ and H₂O, commonly referred to as methane oxidation.^{9,10} For the catalytic decomposition of methane, palladium-based catalysts stand out as the most effective metal catalyst among noble metals.^{11–15} The reported methane activation barrier for PdO(100) and Pd(111) surfaces ranges from 1.0 eV to 1.6 eV.^{16–19} The nanoclusters of noble metal often exhibit exceptional catalytic activity due to

the coordinatively unsaturated nature of individual clusters, which enhances the activation of reactants.^{20–23} Additionally, methane activation on pure Transition-metal (TM) surfaces, including noble metals such as Pt, Ru, Rh, and Pd, is notably challenging due to their low reactivity. TM-based catalysts supported on oxides such as cerium-based oxides (CeO_2) gained attention for their cost-effectiveness and enhanced performance for methane oxidation reactions.^{24,25} A DFT study on a palladium cluster supported on CeO_2 demonstrates that the Pd cluster changes its oxidation states, thereby reducing the activation barrier.²⁶ In addition to it, several theoretical studies reported the methane activation barrier on the TM supported CeO_2 less than 1 eV.^{27–29} Mao et. al. conducted a comprehensive study on methane oxidation using palladium nanoparticles featuring pristine and oxygen-coated surfaces and they reported that during the catalytic process of methane oxidation, palladium particles undergo partial oxidation to form PdO .^{30,31} A recent experimental study revealed that during the methane oxidation, the likelihood of Pd metal transitioning to PdO increases with a higher CH_4/O_2 ratio or a decrease in temperature, leading to a substantial enhancement in the catalytic activity for methane oxidation.^{32,33} Iglesia et. al. have demonstrated that turnover rates increase as Pd clusters undergo bulk oxidation, forming PdO clusters.³⁴

Moreover, the catalytic activity of these Pd-based catalysts is highly dependent on the nature of the support material, the oxidation state, and the stability of palladium species and their interaction with the support and environmental elements.^{35–38} Oxygen is one of the co-reactants of CH_4 and plays a crucial role in its complete oxidation as an environmental element.³⁹ Importantly, the presence of both Pd and PdO on the particle surface serves to lower the activation energy required for methane oxidation effectively but there is still debate about which is better of them.^{40–42} Some studies suggest that metallic Pd is more effective than PdO in the complete oxidation of methane.^{42,43} However, recent research points to PdO_x or a metal/oxide interface as the key to catalytic activity.⁴⁴ These differing conclusions may arise from the dynamic coexistence of Pd and PdO during reactions, making it difficult to pinpoint specific active structures and establish clear structure-activity

relationships. PdO nanostructure shows good stability with the metal oxide surfaces such as CO_3O_4 ,^{45,46} CeO_2 ,⁴⁷ NiO ,⁴⁸ MgO ,⁴⁹ ZnO ,^{50,51} Al_2O_3 ,^{52,53} graphene oxide⁵⁴ and zeolite.⁵⁵ Wolf et. al. reported that the PdO/ CeO_2 nanostructure exhibits high catalytic activity for low-temperature methane oxidation and the presence of water significantly reduces the activity.⁴⁷ Some experiments show that in excess presence of O_2 , Pd single atoms are readily activated into PdO_x single nanocluster which helps to boost the catalytic activity for methane oxidation.⁵⁶

Apart from this, understanding complex reaction mechanisms is essential for designing better catalysis in heterogeneous catalysis. While recent advances in in-situ experiment techniques have improved our ability to study the catalytic reaction, tracking complete reaction pathways remains challenging, especially when multiple competing mechanisms are involved. In such cases, first principle calculations paired with microkinetic modeling offer a valuable approach to exploring reaction kinetics.^{57–60} In this study, we explored the complete reaction pathways of a single PdO_x cluster supported on the $\text{CeO}_2(111)$ surface for methane oxidation using density functional theory (DFT). The $\text{CeO}_2(111)$ surface was selected for its well-established stability and enhanced reactivity.^{61,62} Additionally, we investigated the reaction path selectivity, production rate, degree of rate control, and turnover frequency through microkinetic modeling.

Computational Methodology

First-principles study

This investigation employs first-principles calculations using density functional theory (DFT)^{63–65} within the Vienna Ab initio Simulation Package (VASP).⁶⁶ The Perdew-Burke-Ernzerhof (PBE) method is chosen for exchange-correlation energy, while the projected augmented wave (PAW) method⁶⁷ describes the core-valence electron interaction. A plane wave basis set with an energy cutoff of 500 eV is employed, and the Brillouin zone is sampled using

a $4 \times 4 \times 1$ k-points mesh. A U value of 5 eV is applied to the Ce f-orbitals, as used in earlier theoretical studies.⁶⁸ Additionally, we incorporate the semi-empirical D3 van der Waals (vdW) correction to enhance the description of the adsorbed system,⁶⁹ and charge transfer is determined using the Bader charge analysis method.⁷⁰ The study focuses on the (111) surface of CeO₂, known for its good reactivity and stability.^{71–73} The CeO₂(111) surface is modeled with a $1 \times 1 \times 1$ conventional unit cell consisting of 4 layers (12 O-Ce-O atomic sublayers with 16 CeO₂ units). Following the benchmark tests, we decided to use a $1 \times 1 \times 1$ conventional unit cell for this study, rather than a larger supercell, as outlined in our previous work.⁷⁴ The lattice constant of this surface is 7.68 Å, with a thickness of 10.7 Å, which we used throughout our calculations, and an additional 18 Å vacuum along the z-direction to minimize interactions between periodic images. The bottom six atomic layers are fixed, while the upper six layers can relax until the maximum forces on each atom are below 0.005 eV/Å. To identify the most stable sites for the adsorption of single Pd and PdO, the adsorption energy (E_{ads}) is calculated using the formula; $E_{ads} = E_{surface + adsorbate} - E_{surface} - E_{adsorbates}$, where each term refers to the DFT calculated total energy of the respective system. The thermodynamic behavior of each intermediate reaction step during methane oxidation is analyzed by computing the enthalpy change (ΔH) as the difference between the DFT-calculated total energies of the product and reactant: $\Delta H = E_{product} - E_{reactant}$. The activation barrier (E_a) is determined using the climbing image nudged elastic band (CI-NEB) method,⁷⁵ which is considered as the difference between the total energy of the transition state (TS) and the initial state (IS); $E_a = E_{TS} - E_{IS}$. Additionally, we developed a Brønsted–Evans–Polanyi (BEP) relationship to estimate the reaction barriers of intermediate steps involved in methane oxidation (see Supporting Information).

Microkinetic Modelling

The microkinetic modeling was performed using the MKMCXX software,⁷⁶ with the assumption that all adsorbed species occupy a single position. For surface reactions, the rate

constant of the forward and reverse reactions can be derived from the Eyring equations, $k = \frac{K_B T}{h} \exp\left(-\frac{\Delta G^\ddagger}{RT}\right)$, where, k is the reaction rate constant, ΔG^\ddagger is the Gibbs free energy, R is the gas constant and T is the temperature in Kelvin, respectively. The following equation is used to calculate the adsorption and desorption rates,

$$K_{ads} = \frac{PA}{\sqrt{2\pi m K_b T}} S \quad (1)$$

and the

$$K_{des} = \frac{K_b T^3}{h^3} \frac{A(2\pi m K_b)}{\sigma \theta} e^{-E_{des}/K_b T} \quad (2)$$

Where, P , A , m , S , σ , θ and E_{des} denote the partial pressure, the surface area of the adsorption site, relative molecular mass, the sticking coefficient, the symmetric number, rotational characteristics temperature and the desorption energy, respectively. The value of symmetry number (σ) for CH_4 , O_2 , CO_2 , H_2O is 12, 2, 2, 2⁷⁷ and rotational temperature (θ) for CH_4 , O_2 , CO_2 , H_2O is 7.54 K, 1.47 K, 0.56 K, 20.9 K, respectively.⁷⁷⁻⁷⁹ To simplify our simulations, the sticking coefficients were set to 1 throughout all microkinetic simulations.^{80,81} The apparent activation energy can be calculated from the equation

$$r = k_{ads} \cdot p_A - k_{des} \cdot [A_{ads}] \quad (3)$$

$$E_{app} = RT^2 \frac{d \ln r}{dT} = -R \frac{d \ln r}{d \frac{1}{T}} \quad (4)$$

$$X_{c,i} = \frac{k_i}{r_c} \left(\frac{\partial r_c}{\partial k_i} \right) k_j = \left(\frac{\partial \ln r_c}{\partial \ln k_i} \right) \quad (5)$$

where r is the total rate of the equation and T is the temperature. The degree of rate control (DRC) refers to the relative change of the rate caused by the rate constant of a given elementary reaction step while keeping the equilibrium constant.

Results & Discussion

This work is divided into two main sections. First, we analyzed the complete reaction pathways using DFT, followed by a discussion on production rates, turnover frequency, and the degree of rate control based on microkinetic modeling. The DFT analysis is further divided into two parts: investigating the direct and indirect effects of oxygen through Pd and PdO supported by CeO₂(111). In the first part, we examined the interaction between PdO and CeO₂ (direct effect). In the second part, we studied how O₂ interacts with a single Pd atom to form PdO_x species (indirect effect). The complete reaction pathways for Pd1@CeO₂ under dry conditions have already been investigated by our group.⁷⁴ In this study, we focus specifically on the reaction pathway for Pd1@CeO₂ under oxygen-rich conditions.

Adsorption of Pd and PdO over CeO₂(111)

We chose four distinct sites, as depicted in Figure 1 (in the middle), to study the adsorption of Pd and PdO on the CeO₂(111) surface. In addition to examining the adsorption sites, for PdO, we also investigated the orientation during adsorption by considering both Pd and O facing toward the surface. All possible adsorption sites and orientations of PdO have been depicted in SFig1. The adsorption energies of all possible sites and orientation for Pd and PdO adsorption are mentioned in the table.1 in the supporting information. For both Pd and PdO, the most stable adsorption site is the bridge site (site 4), with adsorption energies of -2.24 eV for Pd and -2.99 eV for PdO, indicating a stronger interaction of PdO with the surface compared to a single Pd atom. These adsorption energies agree with previously reported values.^{74,82,83} In case of PdO, the orientation of Pd towards the surface is the most stable geometry as compared to O towards the surface. The Pd of PdO is connected with O_S on the surface and constructs PdO₂ local species.

The optimized Pd1@CeO₂ and PdO1@CeO₂ structures at the most stable site have been shown in Figure 1 (a) & (c), respectively. In our previous work, we reported the adsorption of

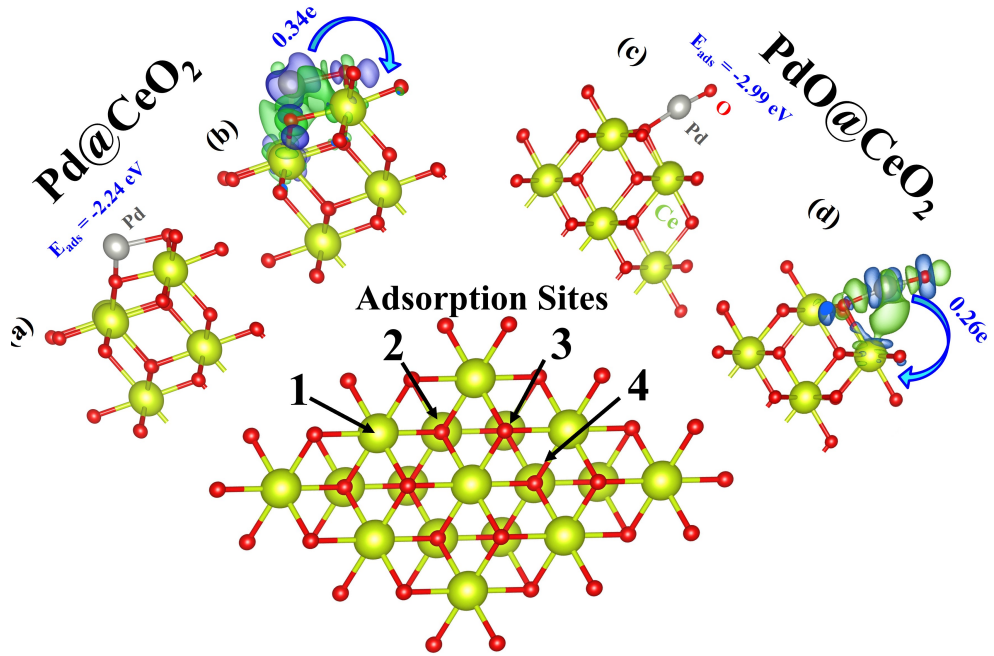


Figure 1: The adsorption site for single Pd and PdO over the optimized CeO_2 supercell (in the middle), where 1, 2, 3 and 4 refers to the top of Ce atom, top of oxygen, top of hexagon and bridge of Ce & O. The relaxed geometry/charge transfer of $\text{Pd}1@\text{CeO}_2$ and $\text{PdO}1@\text{CeO}_2$ in (a)/(b) and (c)/(d), respectively. The green and blue colors indicate the accumulation and depletion of electrons.

a single Pd atom on the CeO₂ surface.⁷⁴ In this study, we focus primarily on the adsorption of PdO on the CeO₂(111) surface. The variance in adsorption energy of PdO compared to the top of the oxygen site (site 2) and the top of the hexagon site (site 3) is 0.37 eV and 0.36 eV, respectively. Upon adsorption of PdO on the CeO₂ surface, the Pd-O bond length reduces to 1.79 Å, slightly shorter than that in the PdO molecule (1.81 Å), with a distance of 1.97 Å from the surface. The O atom of PdO is slightly bent towards the Ce atom at the surface. Similar to a single Pd atom, PdO also bonds with two oxygen atoms; one from the PdO molecule and the other from the CeO₂ surface, forming a PdO₂ local species by changing its oxidation state from Pd⁰ to Pd⁺², which is more catalytically active. Through the Bader charge analysis, it was confirmed that during the adsorption, both Pd and PdO transfer 0.34e and 0.26e charges to the surface, reducing Ce⁴⁺ to Ce³⁺ as shown in Figure 1(b) & (d).

Intermediate Species in Associative and Dissociative form on PdO@CeO₂

When considering the adsorption of carbon species in its associative form on the PdO1@CeO₂(111) surface, there exists a competition between two sites: Pd and O as shown in Figure 1(c). We compared the adsorption energy for each carbon species on both sites, and it was found that the 'Pd' site is thermodynamically more catalytically active. The adsorption energies for all carbon species on both the 'Pd' and 'O' active sites are provided in Table 1 in the supporting information. The optimized structural geometries of the intermediate species adsorbed on PdO1@CeO₂ are illustrated in their associative form in Figure 2 and in their dissociative form in SFig3

In the case of methane (CH₄) adsorption, methane is physisorbed over Pd1/CeO₂(111) in a scissor geometry, with an adsorption energy of -0.21 eV, similar for both sites. The adsorption of methane retains the surface geometry while pushing the PdO molecule closer to the surface, where the oxygen atom of PdO forms a bond with the Ce atom of the surface at a bond length of 2.43 Å as shown in Figure 2(a). The distance between methane and

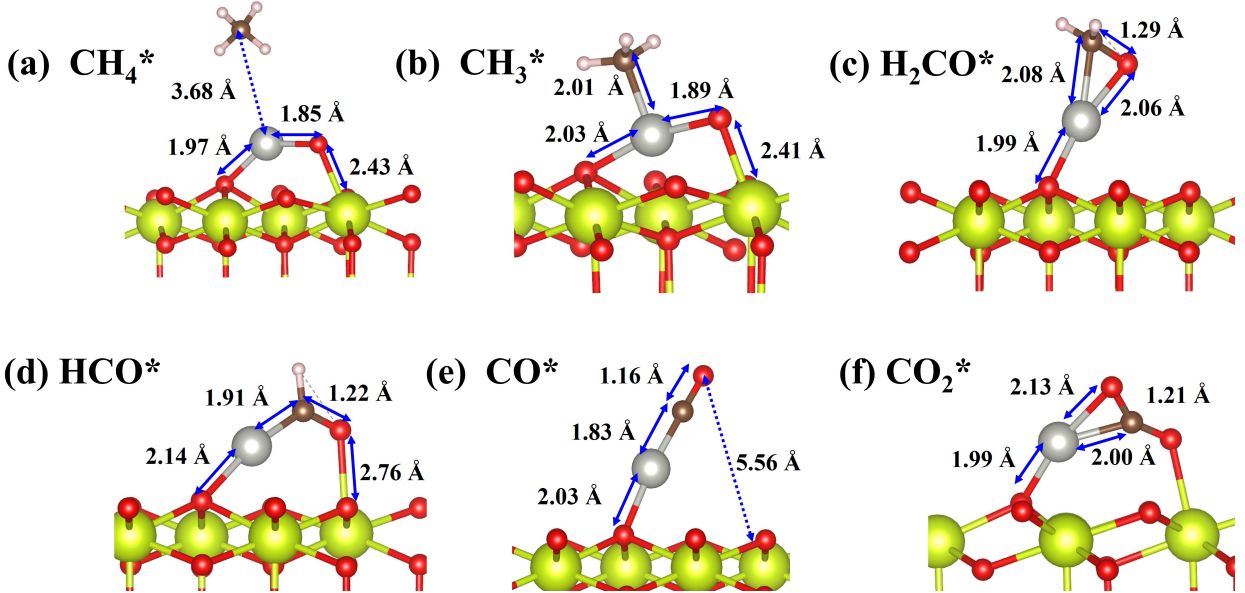


Figure 2: Geometrical representation of adsorbed carbon species in the associative form on PdO supported with $\text{CeO}_2(111)$ surface; (a) CH_4^* , (b) CH_3^* , (c) H_2CO^* , (d) HCO^* , (e) CO^* , and (f) CO_2^* .

the Pd atom measures 3.68 \AA . However, in the case of CH_3 adsorption, the adsorption energies are -2.03 eV and -2.97 eV for the Pd and O sites, respectively. According to the Sabatier principle, the Pd site proves to be thermodynamically more favorable compared to the 'O' site. Additionally, the adsorption of CH_3 further suppresses PdO towards the surface, bonding with the Pd atom in an umbrella-style configuration, with a distance of 2.01 \AA between the CH_3 molecule and the Pd atom, which can be seen in Figure 2(b). Following the adsorption of CH_4 and CH_3 species, there's a localized formation of PdO_2 species. Similar to CH_3 , both CH_2 and CH species also exhibit a preference for the Pd site, displaying adsorption energies of -5.94 eV and -7.88 eV , respectively, which are notably lower than those of -0.20 eV and -1.30 eV observed for the O site. The adsorbed CH_2 species form bonds with both Pd and oxygen atoms, with the carbon positioned at a distance of 2.08 \AA from Pd and 1.29 \AA from oxygen. Similarly, CH also bonds with Pd and O atoms, with the carbon situated at distances of 1.91 \AA and 1.22 \AA , respectively. The adsorption energy for single C and H is the same for both the Pd and O sites (See Table. 1, in supporting information).

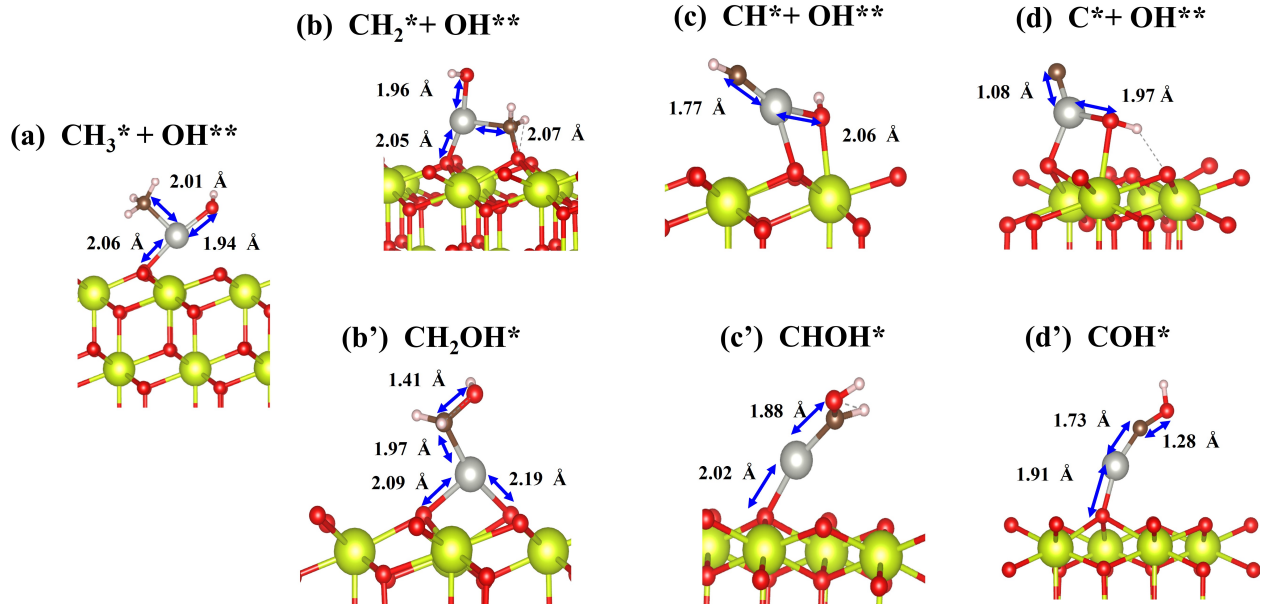


Figure 3: The optimized geometries of other intermediates over $\text{PdO}@\text{CeO}_2$ during methane oxidation. The '*' and '**' show the Pd and O as the adsorption sites. The (b), (c), (d) and (b'), (c'), (d') represent the intermediate species for path1 and path2.

In addition to the adsorption of species in their associative form, we also examined the intermediate species in their dissociative form during methane oxidation as shown in Figure 3, where 'Pd' and 'O' were considered as the active sites. Upon dissociation of CH_4 , CH_3^* bonds to Pd and H^{**} bonds to O, where '*' and '**' represent their attachment to Pd and O, respectively. The bond distances are 2.01 Å for CH_3^* to Pd and 1.01 Å for H^{**} to O, which is comparable to the OH bond length. This confirms that CH_4 dissociates into CH_3 and OH ($\text{CH}_4 \rightarrow \text{CH}_3^* + \text{OH}^{**}$) as depicted in Figure 3(a). During CH_3 dissociation, two stable intermediates were identified: $\text{CH}_2^* + \text{OH}^{**}$ and CH_2OH^* . In both cases, Pd maintains the same coordination, bonding with two oxygen atoms and one carbon atom. These two stable intermediates proceed along two different reaction pathways with distinct intermediates: $\text{CH}_2^* + \text{OH}^{**} \rightarrow \text{CH}^* + \text{OH}^{**} \rightarrow \text{C}^* + \text{OH}^{**}$ (in Figure 3(b)-(d)), and $\text{CH}_2\text{OH}^* \rightarrow \text{CHOH}^* \rightarrow \text{COH}^*$ (in Figure 3(b')-(d')). In the $\text{CH}^* + \text{OH}^{**}$, the Pd atom forms a bond with CH^* at a distance of 1.77 Å, while OH is 2.06 Å away from Pd and in the CHOH^* , the distance between Pd and CHOH^* is 1.88 Å, showing that Pd bonds more strongly with

CH^* compared to CHOH^* . Thus, during the dissociation of CH^* to $\text{C}^* + \text{OH}^{**}$ and CHOH^* to COH^* , Pd exhibits coordination numbers of 3 and 2, respectively. The C^* species bonds more strongly with Pd compared to COH^* .

Reaction pathway for Methane Oxidation at $\text{PdO}_1@\text{CeO}_2$

Our primary focus was on the dissociation of methane into CO_2 , and we investigated the reaction pathway of methane dissociation over the $\text{PdO}_1@\text{CeO}_2(111)$ surface. As we found two active sites over the $\text{PdO}_1@\text{CeO}_2(111)$ surface, the active site O assumes a crucial role, exhibiting two distinct reaction pathways. In one pathway, it continues to act as an active site, while in the other, it undergoes a change in behavior, transitioning from an active site to an element of the product. Both reaction pathways are shown in Figure 4 with the reaction energy of their respective reaction steps and the intermediates of these paths can be seen in Figure 5. The thermodynamic behavior of both reaction pathways is different, and there are notable differences in their reaction energies. This discrepancy aids in determining the preferred reaction pathway for methane dissociation into CO_2 .

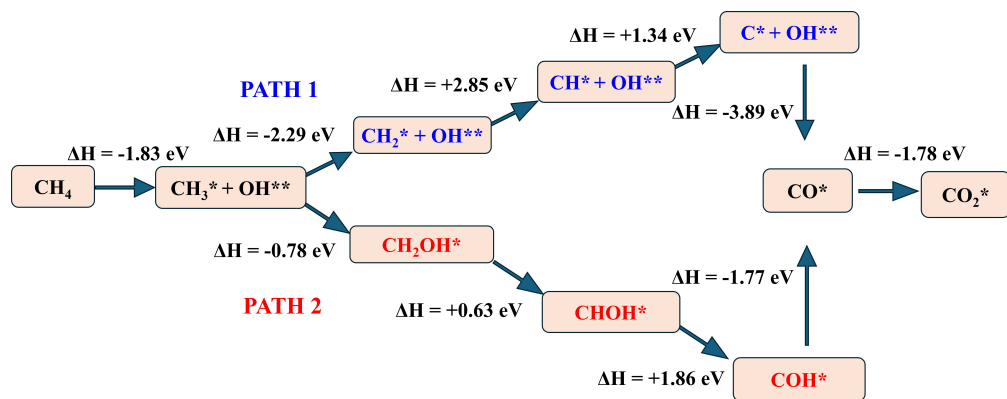


Figure 4: Two distinct reaction pathways with respective Gibbs free energy for methane conversion into CO_2 over $\text{PdO}_1@\text{CeO}_2(111)$. Some intermediates are common in both path 1 (blue color) and path 2 (red color).

The first step for both reaction pathways is similar as represented in Figure 4, where methane is initially physisorbed on the surface and undergoes an exothermic reaction with

a reaction energy of -1.83 eV. Subsequently, the methane molecule breaks into CH_3^* and H^{**} species, with CH_3^* bonding with Pd and H^{**} species bonding with O. These bonding preferences correspond to the respective thermodynamically favorable sites discussed in the previous section. The required energy barrier to break CH_4 on PdO1@CeO_2 is 0.63 eV, calculated using a nudged elastic band method with DFT. In the second step of the reaction path, which involves removing the second hydrogen from the CH_3^* species, two distinct products are formed $\text{CH}_2^*+\text{OH}^{**}$ and CH_2OH^* in reaction path 1 and reaction path 2, respectively. During the formation of $\text{CH}_2^*+\text{OH}^{**}$, CH_2^* is situated on the Pd active site while H^{**} is located on the O active site, as depicted in the third box in path 1 in reaction pathways 1. This process exhibits thermodynamically exothermic behavior with a reaction energy of -2.29 eV. The third step $\text{CH}_2^* \rightarrow \text{CH}^* + \text{OH}^{**}$ and fourth steps $\text{CH}^* \rightarrow \text{C}^* + \text{OH}^{**}$ of reaction path 1 are thermodynamically endothermic with reaction energy +2.85 eV and +1.34 eV.

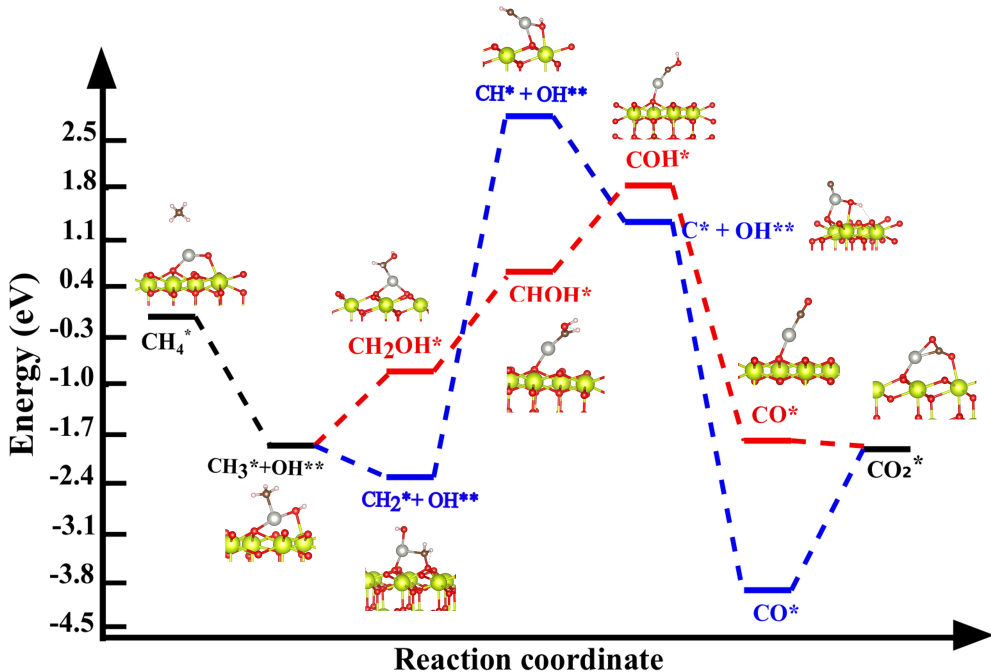


Figure 5: Complete reaction pathways for methane dissociation into CO_2 over $\text{PdO1@CeO}_2(111)$. Blue and red colors refer to Path 1 and Path 2, whereas black color represents the common intermediates in Path 1 and Path 2. The '*' and '**' depicted the Pd and O as an active site.

In pathway 2 of the reaction, the energy barrier for the reaction is notably lower compared

to pathway 1 due to the formation of a different product. In the second step of pathway 2, we observe the formation of alcohol after releasing 0.78 eV of energy, showing the exothermic behavior, whereas in the third step, the formation of alcohol occurs after absorbing +0.63 eV of energy, demonstrating a thermodynamically endothermic behavior.

Reaction Pathway for Methane Oxidation at Pd1@CeO₂ in Oxygen-rich Condition

In our work, we focused on the role of oxygen in both direct and indirect approaches during methane oxidation. The previous section focused on methane oxidation over a single PdO supported on the CeO₂(111) surface, specifically investigating the direct role of oxygen as PdO. In this section, we will discuss the indirect approach, where O₂ interacts with CH₄ to form a local PdO_x geometry that serves as an active site. This method is referred to as methane oxidation in oxygen-rich conditions, as the dissociation of methane occurs in the presence of oxygen. In our earlier work, we already studied methane dissociation in the absence of oxygen, known as dry conditions or deep dehydrogenation.⁷⁴ The complete reaction pathway for methane dissociation into CO₂ in the presence of oxygen is depicted in Figure 6, and a structural representation of this process can be seen in SFig.3. (See Figures S4, S5, and S6 in the supporting information for the possible configurations of intermediate species adsorbed on the Pd@CeO₂ surface).

During our investigation of methane oxidation in oxygen-rich conditions, we found that CH₄ and O₂ compete for adsorption on the active site, as both molecules tend to bond with Pd. When O₂ adsorbs on Pd1@CeO₂, it binds symmetrically with Pd, forming localized PdO₂ species. The adsorption energy of the O₂ molecule is -1.63 eV, indicating a stronger binding with Pd compared to CH₄, which has an adsorption energy of -0.21 eV. The bond length between the oxygen atoms in O₂ extends from 1.20 Å (in the isolated molecule) to 1.31 Å (after adsorption over Pd1@CeO₂), while the distance of both oxygen atoms from

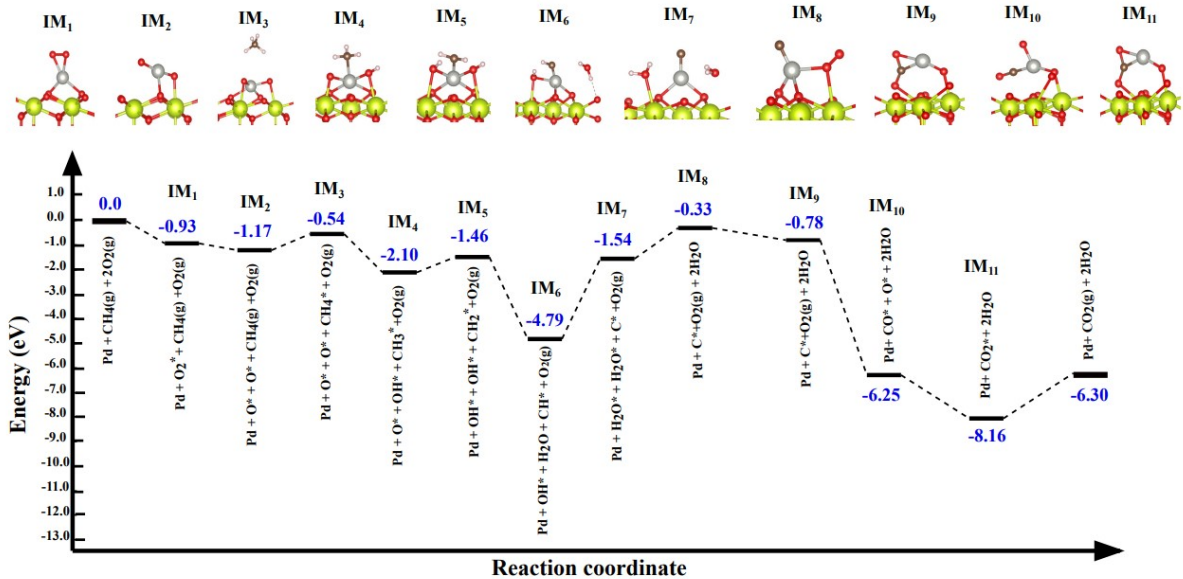


Figure 6: The complete reaction pathways of methane oxidation over $\text{Pd}@\text{CeO}_2(111)$ in the presence of oxygen with the structural view of corresponding intermediates.

Pd is 2.03 \AA . Upon O_2 adsorption on $\text{Pd}@\text{CeO}_2(111)$ surface, it undergoes an exothermic reaction, indicating thermodynamic favorability with a reaction energy of -0.92 eV . In the subsequent step, the adsorbed oxygen molecule dissociates into two individual O^* atoms, which then act as active sites in the methane dissociation process. The dissociation of oxygen also is a thermodynamically exothermic reaction with an energy of -1.17 eV . The activation barrier for O_2 dissociation is 2.12 eV , which lies in the range of previous values.^{84,85} During the dissociation, the distance between the dissociated oxygen atoms increases from 1.31 \AA (before dissociation) to 2.87 \AA , with one oxygen atom elongating towards the surface Ce atom. The bond length of the dissociated oxygen atoms from Pd is 1.79 \AA and 1.87 \AA . After the dissociation of O_2 , the next step of the reaction path is the dissociation of methane, where dissociated O^* acts as an active site for methane adsorption. The adsorption of CH_4 causes the PdO_2 species to be pushed toward the surface, while Pd forms additional bonds with two oxygen atoms from the surface. The methane molecule breaks down into CH_3 and H, where CH_3^* binds to the Pd atom and H binds to the oxygen atom of O_2 , forming the OH^* species, as depicted in Figure 6. The dissociation of methane over $\text{Pd}@\text{CeO}_2(111)$ exhibits

an exothermic nature thermodynamically with a reaction energy of -2.10 eV.

Similarly, CH_3^* , CH_2^* , and CH^* undergo stepwise dehydrogenation, leading to the sequential formation of OH^* and H_2O^* species. Once the water species is formed, it weakly bonds to the surface before desorbing, leaving behind the C^* species, which can be seen in Figure 6. Once the water molecule is eliminated, the remaining carbon species obstruct the active Pd site. Subsequently, an O_2 molecule adsorbs onto the Pd surface and dissociates in the presence of the C^* species. The dissociation of O_2 required for the subsequent formation of CO_2 as a product becomes significantly difficult. The presence of adsorbed C^* on top of Pd resulted in a slowed dissociation process. Upon comparing the adsorption energies of O_2 molecules in the absence and presence of carbon species at the Pd site, we observed a significant weakening of the O_2 molecule's bonding in the presence of carbon species, leading to a reduction in adsorption energy by more than half. Specifically, in the absence of C^* at Pd, the adsorption energy measured -0.89 eV and bond length 1.34 Å, which is elongated as compared to isolated O_2 molecule. While in the presence of C^* at Pd, the adsorption energy of the O_2 molecule decreased to -0.42 eV and the bond length was 1.29 Å which is almost similar to the isolated molecule which concludes that in the presence of C^* , the O_2 molecule is less activated for the dissociation. In summary, the steps involved in methane oxidation can be described as follows, (i) the adsorption of methane on Pd1@CeO_2 surface in the presence of O_2 ; ($\text{Pd}+\text{CH}_4(\text{g}) \rightarrow \text{Pd}+\text{CH}_4^*$); (ii) removing of hydrogen step by step from CH_4^* , CH_3^* , CH_2^* , and CH^* species ($\text{CH}_4^* \rightarrow \text{O}^*+\text{OH}^*+\text{CH}_3^* \rightarrow \text{OH}^*+\text{OH}^*+\text{CH}_2^* \rightarrow \text{O}^*+\text{OH}^*+\text{CH}^* \rightarrow \text{H}_2\text{O}^*+\text{H}_2\text{O}^*+\text{C}^*$); (iii) desorption of H_2O and CO_2 molecules ($\text{H}_2\text{O}^*+\text{H}_2\text{O}^*+\text{C}^* \rightarrow \text{C}^*+2\text{H}_2\text{O}(\text{g}), \text{CO}_2^* \rightarrow \text{CO}_2(\text{g})$) as depicted in Figure 1 in supporting information (refer to this figure for a more detailed understanding, as it highlights all intermediates along with their structural views).

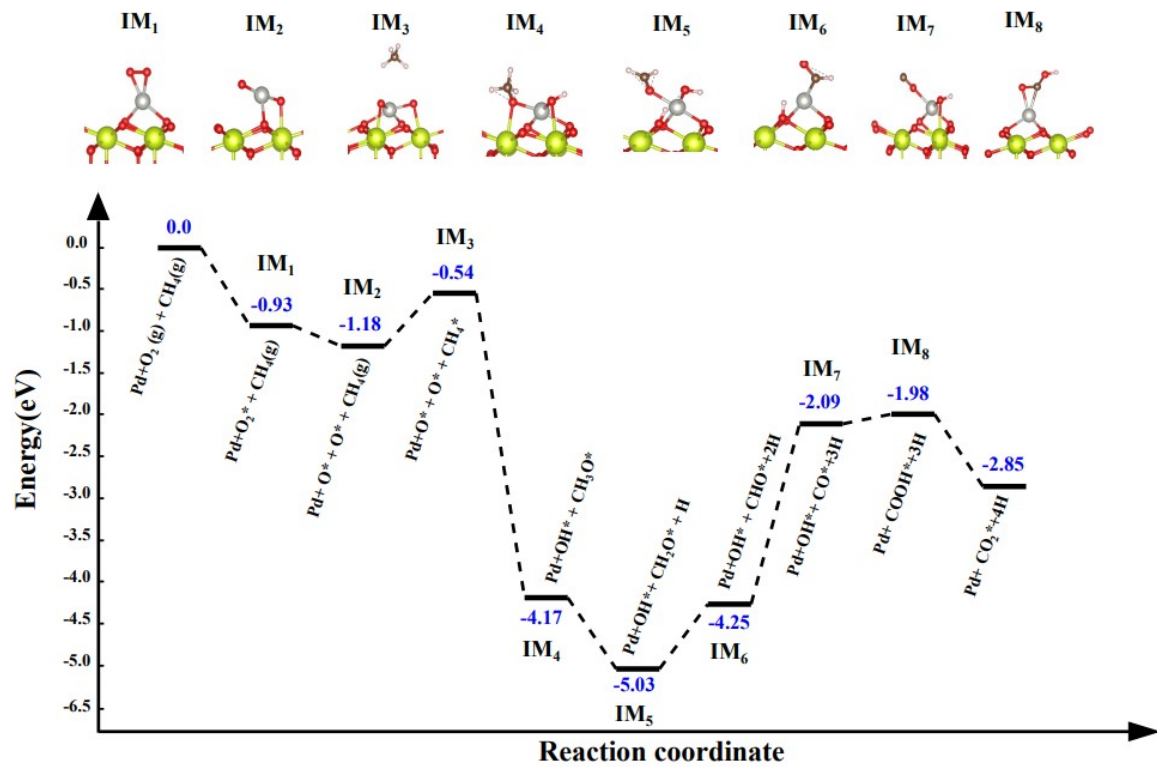


Figure 7: The alternate reaction pathways of methane conversion into CO₂ on Pd1@CeO₂(111) in presence of oxygen with the structural view of corresponding intermediates.

Alternate way for CO₂ Formation

The complete reaction pathways for methane oxidation in oxygen-rich conditions were discussed in detail in an earlier section. Out of all the reaction steps, some of them are thermodynamically unfavorable, as represented in Figure 6. Therefore, we tried to investigate the alternate path of CO₂ formation which shows more thermodynamical favorability. The alternate reaction path for CO₂ formation has been shown in Figure 7, which shows the conversion of CH₄ molecule in the presence of O₂ into CO₂ and H₂. The total Gibbs free energy during the complete oxidation of methane is -2.8 eV which is lower than the previous path (-6.3 eV). In this reaction pathway, after methane dissociates on the surface over two dissociated O* species acting as active sites, both CH₃* and H* bind to the dissociated O* species, forming CH₃O* and OH*, respectively. Following the formation of OH*, the next hydrogen atom is removed from CH₃* and bonds with the surface rather than the active site. The reaction proceeds with CH₃O* transforming stepwise into CH₂O*, CHO*, and eventually CO*. After CO* and OH* are formed, they combine to form COOH*, which, upon the removal of one hydrogen, produces CO₂.

Role of Lattice Oxygen during CO Formation

In our previous study, we reported the complete reaction path for methane oxidation without taking into account the lattice oxygen as an active site.⁷⁴ Here, we investigated the role of lattice oxygen and discovered that, rather than leading to CO₂ formation, the lattice oxygen played a crucial role in the formation of CO. The formation of CO through methane oxidation is a thermodynamically favorable process with a reaction energy is -11.6 eV and the reaction pathway has been shown in Figure 8, where the dissociation steps of O₂ and CH₄ are identical to the previous reaction path (Figure 6). After CH₄* dissociates on O* species, the formation of two different CH₃O* and OH* occurs spontaneously. Later on, lattice oxygen plays a key role. CH₃O* loses one hydrogen, which bonds with the lattice oxygen, forming OH_s* (where 'OH_s' represents lattice oxygen). Similar to CH₃O*, CH₂O*, and CHO* remove hydrogen

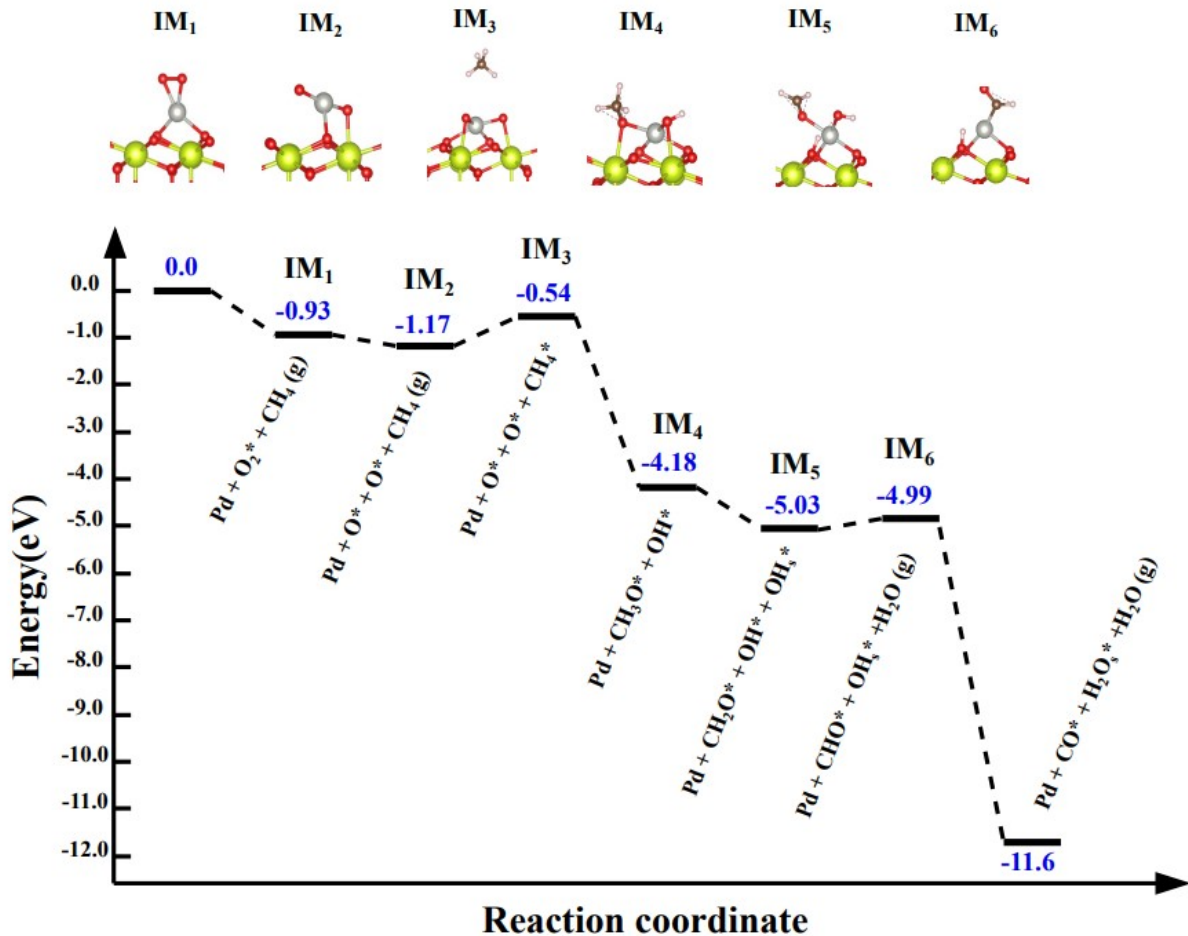


Figure 8: The role of lattice oxygen during methane oxidation. OH and OH_s represent the formed species at the active site Pd and the surface, respectively.

one by one and eventually CO^* is formed.

Microkinetic Modeling of Methane Oxidation on Pd1@CeO_2 and PdO1@CeO_2 : Langmuir–Hinshelwood Mechanism and Reaction Pathway Analysis

In the previous section, we extensively discussed various reaction pathways for complete methane oxidation on $\text{Pd1/PdO1@CeO}_2(111)$ using DFT. Beyond DFT, we also employed microkinetic modeling to analyze the reaction dynamics during methane oxidation. This included examining the reaction rate, production rate, and degree of rate control, utilizing DFT-calculated parameters such as activation barriers, Gibbs free energy, and desorption energies. To provide clearer insight, we simulated the microkinetic model for Pd1@CeO_2 alone, as it features a single pathway with several intermediates that help illustrate the overall reaction. PdO1@CeO_2 follows a Langmuir–Hinshelwood mechanism during the methane oxidation process. Initially, both CH_4 and O_2 are adsorbed onto the surface. O_2 then dissociates into atomic O^* species. CH_4 is subsequently decomposed into C^* and H^* species. The C^* reacts with O^* to produce CO^* , and CO^* again reacts with O^* and forms CO_2 . The dissociated H^* atoms combine with another O^* to form H_2O . The desorption process is not detailed here, as H_2O and CO_2 are released directly into the gas phase. Given the minimal energy barrier for H migration on the Pd surface, it is reasonable to assume that the movement of H on the Pd surface has a negligible impact on the overall reaction cycle.

In Figure 9(a) & (b), the reaction rate and degree of rate control are plotted against temperature. It is observed from the results that methane adsorption leads to much higher reaction rates than O_2 dissociation. The rate of methane adsorption increases exponentially between 600 and 1000 K, after which it levels off. In contrast, the rate of O_2 dissociation rises almost linearly from 700 K to 1300 K. The corresponding rates for associated reaction differ

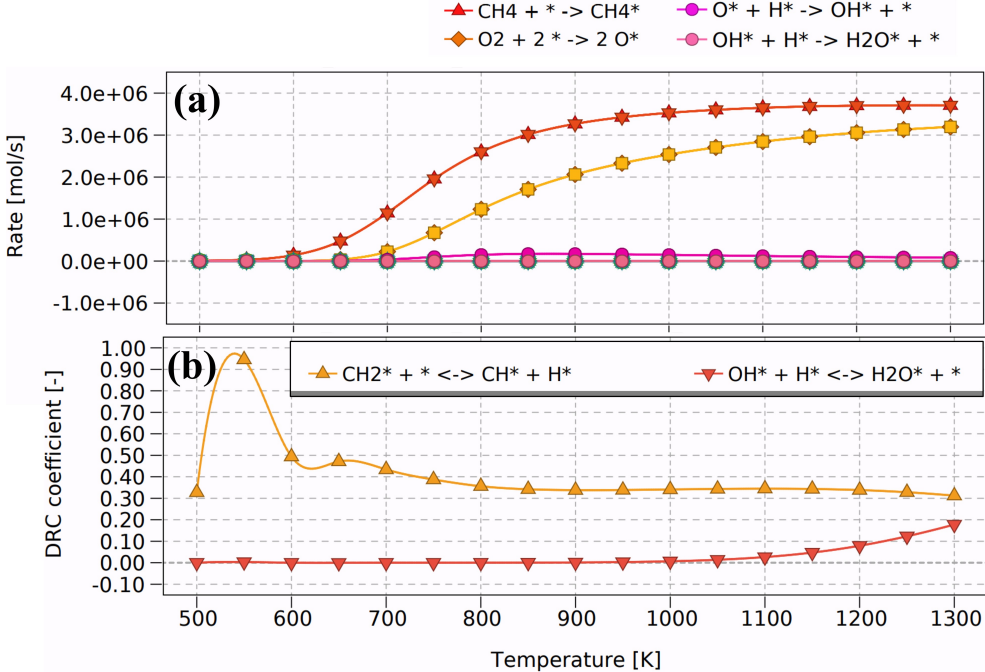


Figure 9: Reaction rate (a) and degree of rate control (b) as a function of temperature (in K) for methane conversion into CO_2 and H_2O on $\text{Pd1@CeO}_2(111)$. These reaction steps play a significant role in controlling the overall reaction rate.

significantly, reflecting a notable variation in the composition of surface species required for the formation of CO_2 and H_2O . In the degree of rate control analysis, we focus on the key reaction steps that play a major role, specifically $\text{CH}_2^* \rightarrow \text{CH}^* + \text{H}^*$ and $\text{OH}^* + \text{H}^* \rightarrow \text{H}_2\text{O}^*$. Among these, the rate control for CH_2 dissociation is significant due to its high activation barrier, indicating that it largely governs the overall methane oxidation reaction. Additionally, the degree of rate control for H_2O^* formation increases only at higher temperatures.

As the rate of each elementary reaction step not only depends on the rate constant but also on the surface coverage of the involved intermediates and the microkinetic modeling provides insight into surface coverages, with the most abundant surface species shown in Figure 10. The surface is primarily covered by O^* and H^* , with oxygen dominating at lower temperatures (around 500 K) and gradually decreasing as the temperature rises. In contrast, hydrogen coverage starts low and steadily increases, eventually covering nearly half of the

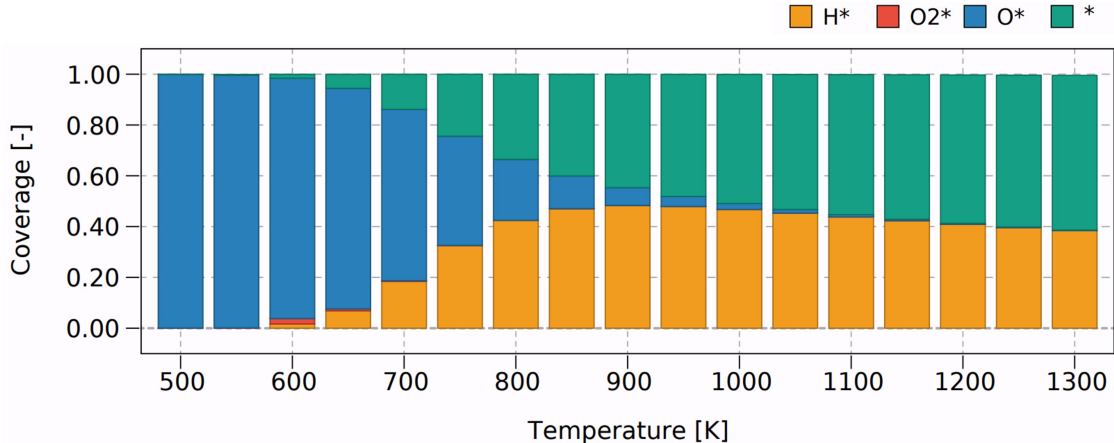


Figure 10: The surface coverage of intermediates as a function of temperature (in K) on Pd1@CeO₂(111)

surface at higher temperatures.

In Figure 11(a) & (b), the selectivity and the production rates of CO₂ and H₂O are plotted concerning the methane oxidation process in the presence of O₂. The selectivity for H₂O formation is higher than CO₂ due to high H* surface coverage, and the selectivity of the product remains constant across different temperatures. At higher temperatures (around 1000 K), CH₄ and O₂ begin to decompose into CO₂ and H₂O. Notably, the decay rate of O₂ is faster than that of CH₄. Moreover, we investigated the apparent activation barrier as a function of temperature, as shown in Figure 12. The apparent barrier exhibits higher values around 500K to 600K, then decreases linearly beyond this range.

To compare the effect of binding between the C* and O* species on the turnover frequency, we plotted the turnover frequency graph with respect to the binding energy of CO* and O*, which is represented in Figure 13. It is worth mentioning that turnover frequency in the presence of oxygen is higher, which indicates that the excess presence of oxygen helps to oxidation of methane into CO₂ and H₂O.

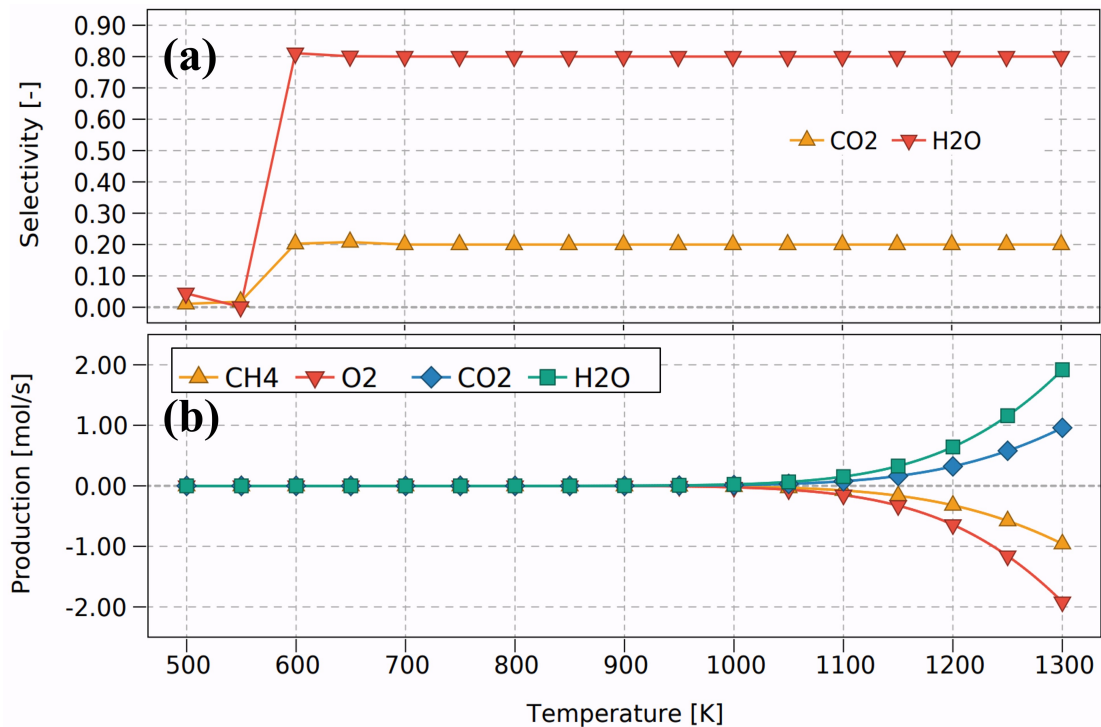


Figure 11: Microkinetic simulation for selectivity (a), production rate (b) as a function of the temperature between 500K and 1300K for products CO₂ and H₂O through the conversion of reactant CH₄ and O₂

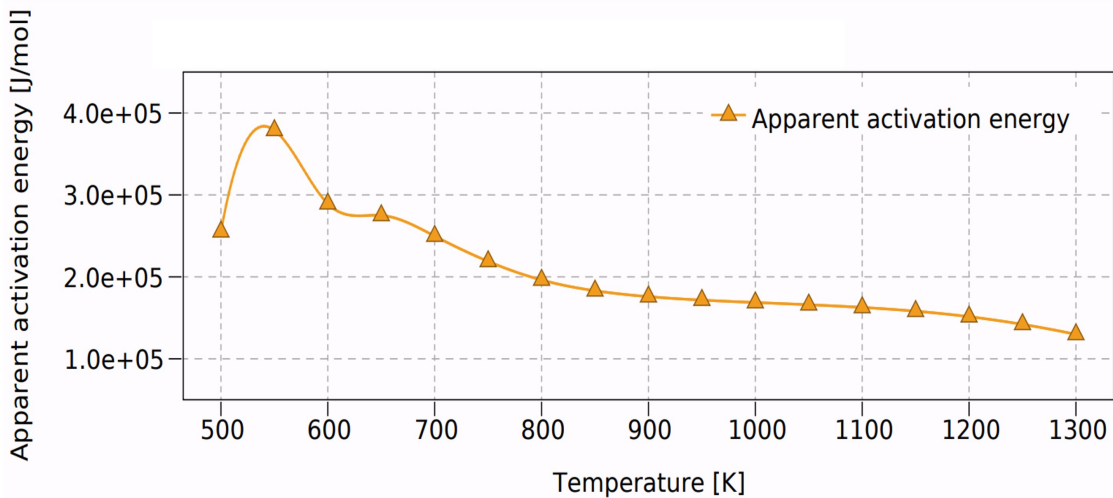


Figure 12: The apparent activation barrier as a function of the temperature (in K) for the methane oxidation into CO₂ and H₂O.

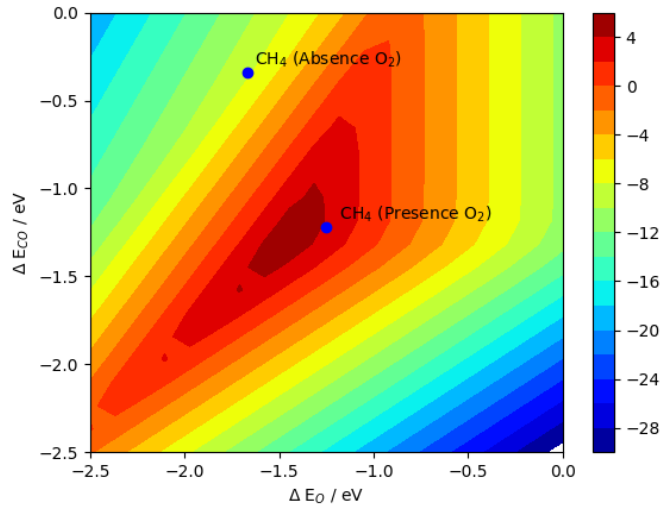


Figure 13: The turnover frequency of CO_2 formation concerning CO^* and O^* binding energy based on microkinetic modeling.

Machine learning of rate constants via symbolic regression using compressed sensing

To model the rate constants for the reaction steps depicted in Figure 6, we employ the Sure Independence Screening and Sparsifying Operator (SISSO) method,⁸⁶ a machine learning approach based on symbolic regression via compressed sensing. This approach is particularly advantageous as it not only provides highly predictive models but also yields interpretable mathematical expressions for the descriptors involved. In the SISSO algorithm, we start with four primary features critical to the reaction kinetics:

- Q_1 : the charge on Pd, representing the electron density on the catalyst surface.
- Q_2 : the charge on the reaction intermediate, indicating its interaction strength with the catalyst.
- Z_N : the coordination number of Pd, reflecting the local geometric environment of the active site.
- d : the distance between the reaction intermediate and Pd, capturing the spatial arrangement affecting orbital overlap.

Table 1: Features and target ($\log(K)$) used for the SISSO study.

Reaction Intermediates	d	Q_1	Q_2	Z_N	$\log(K)$
CH4*	2.68000	9.751262	4.076353	2	37.631182
CH3*	2.00431	9.442062	4.280080	5	97.184808
CH2*	1.83909	9.368178	4.305077	3	152.453042
CH*	1.75211	9.332893	4.276711	3	192.540078
C*	1.64919	8.857009	4.214947	4	184.754929
H*	1.67875	9.378483	1.114597	3	131.042783
O2*	2.00594	9.256038	6.240521	4	45.804522
O*	1.80488	9.057392	6.571158	4	49.294294
OH*	1.98100	9.429129	7.479224	3	109.637353
H2O*	2.23677	9.484897	8.007955	3	111.191914
CO*	1.88227	9.686869	2.415333	3	83.170695

These descriptors capture the essential electronic and geometric properties influencing the rate constants.⁸⁷ The feature space is generated by systematically applying a set of mathematical operators $\mathcal{H}^{(m)} = \{+, -, \times, \div, \sqrt{}, (\cdot)^2, (\cdot)^3, \exp, \sqrt[3]{}\}$ to the primary features, considering up to four iterations. This means that operators are applied recursively up to four times, creating new features from existing ones and expanding the feature space to capture higher-order and nonlinear relationships between the descriptors and the target property.

After four iterations, the recursive application of the operators to the four primary features resulted in a large feature space containing M candidate features. The sensing matrix $\mathbf{D} \in \mathbf{R}^{N \times M}$ is constructed by evaluating these features for each of the N data points in our dataset. Each column of \mathbf{D} corresponds to a specific derived feature, and each row represents a data point with its computed feature values.

The optimization problem solved by SISSO is formulated as:⁸⁸

$$\operatorname{argmin}_{\mathbf{c}} \left(\|\mathbf{P} - \mathbf{D}\mathbf{c}\|_2^2 + \lambda \|\mathbf{c}\|_0 \right), \quad (6)$$

where $\mathbf{P} = [\log(K_1), \log(K_2), \dots, \log(K_N)]$ is the target property vector consisting of the logarithms of the rate constants obtained via micro-kinetic modeling for the shown in the Figure 6. $\mathbf{c} \in \mathbf{R}^M$ is the coefficient vector. λ is the regularization parameter enforcing sparsity. The l_0 norm $\|\mathbf{c}\|_0$ counts the number of non-zero components in \mathbf{c} , promoting a compact and interpretable model.

Limiting the feature construction to four iterations strikes a balance between capturing complex relationships and maintaining model interpretability. While more iterations could generate additional features, they may lead to overfitting and reduce the transparency of the model.

Using the SISSO approach, we successfully generated a 4D descriptor for the $\log(K)$ values, yielding a small error. The final expression is given by:

$$\log(K) = -0.7551 \left(\frac{1}{Q_1 \log(d)} \right) - \frac{3012.5 \cdot Q_2}{Z_N \exp(Q_2)} + 49.91 \left(\frac{Q_2^2}{\exp(Z_N)} \right) + 3726.38 \left(\frac{Q_1 - Q_2}{d^3} \right), \quad (7)$$

Each term in the expression for $\log(K)$ was derived from combinations of the primary features through iterative application of the operators:

The first term $-0.7551 \left(\frac{1}{Q_1 \log(d)} \right)$ captures a nonlinear relationship between the charge on Pd and the geometric factor d . While the second term $-\frac{3012.5 \cdot Q_2}{Z_N \exp(Q_2)}$ involves division and an exponential function, likely arising from higher-order iterations. It highlights the suppressive effect of strong interactions with the intermediate, modulated by the coordination number. The third term $+49.91 \left(\frac{Q_2^2}{\exp(Z_N)} \right)$ includes a squared term and an exponential, indicating a complex relationship derived over multiple iterations. It emphasizes how the charge on the intermediate and the Pd coordination influence K . The fourth term $+3726.38 \left(\frac{Q_1 - Q_2}{d^3} \right)$ combines subtraction, division, and exponentiation, likely from the fourth iteration. It represents the interplay between electronic differences and spatial factors.

Each primary feature in the above expression plays a significant role in influencing the rate constant K , reflecting underlying chemical interactions. For example, Increasing Q_1 raises $\log(K)$, leading to an increase in K . A higher electron density on Pd enhances catalytic activity by facilitating electron transfer processes. Specifically, in the first term, a larger Q_1 reduces the magnitude of the negative contribution $\left(\frac{1}{Q_1 \log(d)} \right)$, thus increasing $\log(K)$. Similarly, in the fourth term, a higher Q_1 contributes positively to $\log(K)$. Similarly, one can see that increasing Q_2 has a dual effect. In the second term, a larger Q_2 increases the magnitude of the negative contribution due to the exponential term $\exp(Q_2)$, potentially decreasing $\log(K)$. However, the third term contains Q_2^2 in the numerator, and increasing Q_2 enhances this positive contribution, which can outweigh the negative effects. Overall, higher Q_2 tends to increase K through its positive squared term, indicating that certain charge states of the intermediate favor reaction progression. It is easily understandable

that a shorter distance enhances the overlap of electronic orbitals between the reaction intermediates and the catalyst surface, facilitating the reaction. In the first term, a larger d increases $\log(d)$, which increases the denominator and increases the magnitude of the negative contribution. In the fourth term, a larger d increases d^3 in the denominator, reducing the positive contribution to $\log(K)$.

From the above, it can be understood that optimizing these variables can significantly increase the reaction rate constant. Understanding how each variable influences K allows for targeted modifications to the catalyst or reaction conditions to enhance performance. An interesting aspect of this model is the balance between the second and fourth terms, which have opposing signs and large coefficients. The second term has a strong negative influence on $\log(K)$, particularly when Q_2 is large, reflecting the suppressive effect of strong intermediate interactions. In contrast, the fourth term has a positive contribution, enhancing the rate constant when the difference $Q_1 - Q_2$ is large or the distance d is small. This balance highlights the interplay between the electronic properties of Pd and the reaction intermediate, along with geometric factors. The performance of the 4D model is summarized in Figure 14, where the predicted $\log(K)$ values are plotted against the reference microkinetic values. The model shows excellent agreement, with an R^2 value of 0.997 and a Root Mean Squared Error (RMSE) of 2.851.

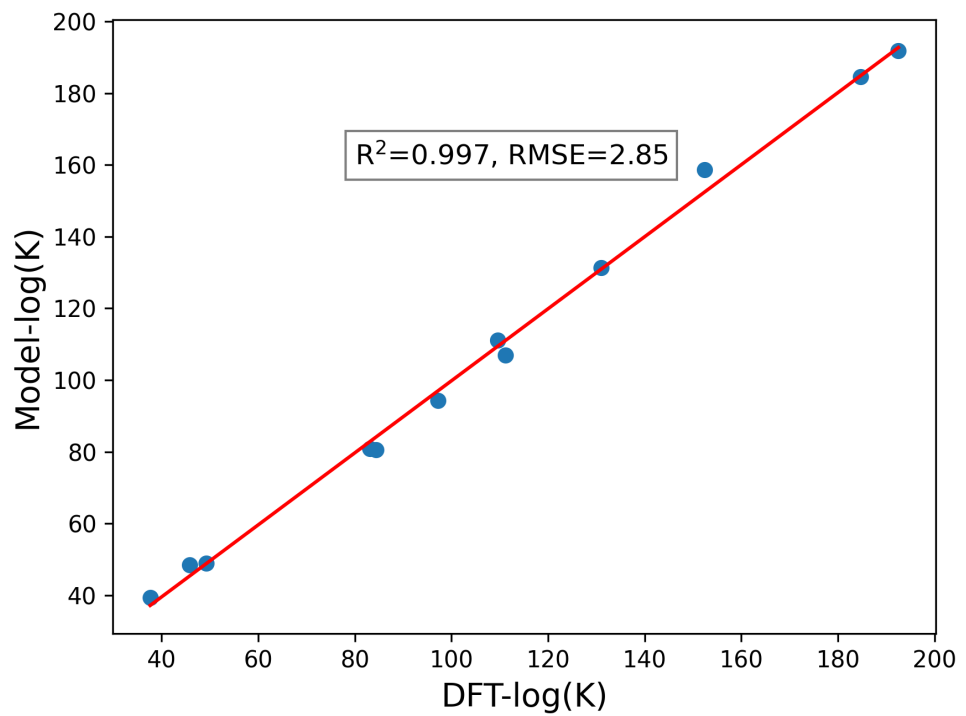


Figure 14: SISSO model performance for the 4D descriptor shown in Eq. 7. The predicted $\log(K)$ values closely match the reference values, demonstrating the model's accuracy.

Direction for the development of new catalysts via insights from the ML model

The four-dimensional descriptor obtained from our SISSO model, comprising the Pd atomic charge (Q_1), the charge on the key CH_xO^* intermediate (Q_2), the local Pd coordination number (ZN), and the Pd–intermediate distance (d)—offers physically interpretable guidance for rational catalyst design. Specifically, the algebraic form of Eq. 7 reveals that high catalytic activity is associated with electron-rich Pd centers that remain in close proximity to moderately charged intermediates. This insight motivates three concrete design strategies. First, the term involving $(Q_1 - Q_2)/d^3$ suggests that activity can be enhanced by maximizing the electronic contrast between Pd and the adsorbate while minimizing the bonding distance. This can be achieved by introducing mild electron-donating dopants into the CeO_2 support or by alloying Pd with more electronegative elements (e.g., Pt, Rh) that enhance Q_1 without significantly altering d . Second, the exponential dependence on ZN in the model indicates that a moderate Pd coordination number ($\text{ZN} \approx 3\text{--}4$) is optimal. Extremely undercoordinated Pd atoms are penalized due to destabilizing effects on transition states, while highly coordinated atoms suppress the favorable interaction terms. This coordination environment is naturally achieved in sub-nanometer Pd clusters or step-edge sites on $\text{CeO}_2(111)$. Third, since overly polarized intermediates with large Q_2 values reduce the rate through the strongly negative exponential term, strategies that stabilize charge-neutral transition states—such as the engineering of oxygen vacancies or doping in the support to control the charge redistribution—can keep Q_2 within the favorable range of 1–3 e^- .

Altogether, the above findings suggest that catalysts incorporating bimetallic PdM (M = Pt, Rh, Cu) clusters supported on vacancy-rich or doped CeO_2 surfaces are promising candidates for optimizing the key descriptors (Q_1, Q_2, ZN, d) identified by our model. This provides a systematic pathway towards the identification of the catalysts with improved performance for methane oxidation, grounded in interpretable machine learning and electronic structure insights.

Conclusions

In conclusion, this study delved into the catalytic mechanism of methane oxidation in the presence of oxygen through two distinct approaches. The first approach involved considering the oxygen-containing molecule PdO, while the second approach focused on the interaction of oxygen as a molecule with single-atom Pd supported with CeO₂(111). Utilizing detailed DFT calculations, we unraveled the complete pathway of methane dissociation into CO₂ under oxygen-rich conditions over Pd1@CeO₂(111). Our results indicate that PdO exhibits favorable thermodynamics for the methane oxidation process over CeO₂(111). This study also highlights the crucial role played by a single Pd atom as an active site for oxygen dissociation, ultimately enhancing catalytic efficiency by reducing the activation barrier for methane oxidation by 0.14 eV. Our findings provide valuable insights into the fundamental processes involved in methane oxidation, which have implications for environmental remediation and industrial catalysis. In addition to the DFT analysis, we examined the apparent activation barrier, degree of rate control, and product selectivity using the microkinetic model. Our results show that surface coverage of H* increases with temperature, which enhances the production of H₂O, as confirmed by the product selectivity. The production CO₂ and H₂ also increase concerning temperature.

Acknowledgement

This work was supported financially by the Fundamental Research Program (PNK9750) of the Korea Institute of Materials Science (KIMS), South Korea. The authors also would like to acknowledge the Param Sanganak, IIT Kanpur supercomputing facility under the National Supercomputing Scheme (CDAC-NSM) for computing time.

Conflicts of interest

The authors declare no conflict of interest.

Supporting Information Available

The supporting information included details of the value of adsorption energy and crystal structural view for different intermediate species on Pd and PdO supported with CeO₂(111) surface in Tab: 1 and Figure 1, Figure 2 & Figure 3, respectively.

References

- (1) Han, Z.; Yang, Z.; Han, M. Comprehensive investigation of methane conversion over Ni(111) surface under a consistent DFT framework: Implications for anti-coking of SOFC anodes. *Applied Surface Science* **2019**, *480*, 243–255.
- (2) Lyubovsky, M.; Pfefferle, L. D. Methane combustion over the α -alumina supported Pd catalyst: Activity of the mixed Pd/PdO state. *Applied Catalysis A-general* **1998**, *173*, 107–119.
- (3) Rouet-Leduc, B.; Hulbert, C. Automatic detection of methane emissions in multispectral satellite imagery using a vision transformer. *Nature Communications* **2024**, *15*, 3801.
- (4) Mao, S.-H.; Zhang, H.-H.; Zhuang, G.-C.; Li, X.-J.; Liu, Q.; Zhou, Z.; Wang, W.-L.; Li, C.-Y.; Lu, K.-Y.; Liu, X.-T.; Montgomery, A.; Joye, S. B.; Zhang, Y.-Z.; Yang, G.-P. Aerobic oxidation of methane significantly reduces global diffusive methane emissions from shallow marine waters. *Nature Communications* **2022**, *13*, 7309.
- (5) Le Mer, J.; Roger, P. Production, oxidation, emission and consumption of methane by soils: A review. *European Journal of Soil Biology* **2001**, *37*, 25–50.

- (6) Liu, H.; Zhang, R.; Yan, R.; Wang, B.; Xie, K. CH₄ dissociation on NiCo (111) surface: A first-principles study. *Applied Surface Science* **2011**, *257*, 8955–8964.
- (7) Burch, R.; Urbano, F.; Loader, P. Methane combustion over palladium catalysts: The effect of carbon dioxide and water on activity. *Applied Catalysis A: General* **1995**, *123*, 173–184.
- (8) Latimer, A. A.; Kulkarni, A. R.; Aljama, H.; Montoya, J. H.; Yoo, J. S.; Tsai, C.; Abild-Pedersen, F.; Studt, F.; Nørskov, J. K. Understanding trends in C–H bond activation in heterogeneous catalysis. *Nature Materials* **2017**, *16*, 225–229.
- (9) Havran, V.; Duduković, M. P.; Lo, C. S. Conversion of Methane and Carbon Dioxide to Higher Value Products. *Industrial & Engineering Chemistry Research* **2011**, *50*, 7089–7100.
- (10) Webley, P. A.; Tester, J. W. Fundamental kinetics of methane oxidation in supercritical water. *Energy & Fuels* **1991**, *5*, 411–419.
- (11) Yin, H.; Pu, Z.; Xue, J.; Ma, P.; Wu, B.; Han, M.; Lin, H.; Luo, Z.; Zeng, J.; Ma, X.; Li, H. Oxygen Vacancy-Rich TiO₂ as an Efficient Non-noble Metal Catalyst toward Mild Oxidation of Methane Using Hydrogen Peroxide as the Oxidant. *ACS Catalysis* **2023**, *13*, 7608–7615.
- (12) Li, X.; Wang, X.; Roy, K.; van Bokhoven, J. A.; Artiglia, L. Role of Water on the Structure of Palladium for Complete Oxidation of Methane. *ACS Catalysis* **2020**, *10*, 5783–5792.
- (13) Li, T.; Beck, A.; Krumeich, F.; Artiglia, L.; Ghosal, M. K.; Roger, M.; Ferri, D.; Kröcher, O.; Sushkevich, V.; Safonova, O. V.; van Bokhoven, J. A. Stable Palladium Oxide Clusters Encapsulated in Silicalite-1 for Complete Methane Oxidation. *ACS Catalysis* **2021**, *11*, 7371–7382.

- (14) Zhu, Y.; Zhang, S.; Shan, J.-j.; Nguyen, L.; Zhan, S.; Gu, X.; Tao, F. F. In Situ Surface Chemistries and Catalytic Performances of Ceria Doped with Palladium, Platinum, and Rhodium in Methane Partial Oxidation for the Production of Syngas. *ACS Catalysis* **2013**, *3*, 2627–2639.
- (15) Willis, J. J.; Gallo, A.; Sokaras, D.; Aljama, H.; Nowak, S. H.; Goodman, E. D.; Wu, L.; Tassone, C. J.; Jaramillo, T. F.; Abild-Pedersen, F.; Cargnello, M. Systematic Structure–Property Relationship Studies in Palladium-Catalyzed Methane Complete Combustion. *ACS Catalysis* **2017**, *7*, 7810–7821.
- (16) Kinnunen, N. M.; Hirvi, J. T.; Suvanto, M.; Pakkanen, T. A. Role of the Interface between Pd and PdO in Methane Dissociation. *The Journal of Physical Chemistry C* **2011**, *115*, 19197–19202.
- (17) Senftle, T. P.; van Duin, A. C. T.; Janik, M. J. Role of Site Stability in Methane Activation on PdxCe1xO Surfaces. *ACS Catalysis* **2015**, *5*, 6187–6199.
- (18) Herron, J. A.; Tonelli, S.; Mavrikakis, M. Atomic and molecular adsorption on Pd(111). *Surface Science* **2012**, *606*, 1670–1679.
- (19) Jørgensen, M.; Grönbeck, H. First-Principles Microkinetic Modeling of Methane Oxidation over Pd(100) and Pd(111). *ACS Catalysis* **2016**, *6*, 6730–6738.
- (20) Kumar, P.; Al-Attas, T. A.; Hu, J.; Kibria, M. G. Single Atom Catalysts for Selective Methane Oxidation to Oxygenates. *ACS Nano* **2022**, *16*, 8557–8618.
- (21) Sun, J.; Tu, R.; Xu, Y.; Yang, H.; Yu, T.; Zhai, D.; Ci, X.; Deng, W. Machine learning aided design of single-atom alloy catalysts for methane cracking. *Nature Communications* **2024**, *15*, 6036.
- (22) Feng, Y.; Wan, Q.; Xiong, H.; Zhou, S.; Chen, X.; Pereira Hernandez, X. I.; Wang, Y.; Lin, S.; Datye, A. K.; Guo, H. Correlating DFT Calculations with CO Oxidation Reac-

- tivity on Ga-Doped Pt/CeO₂ Single-Atom Catalysts. *The Journal of Physical Chemistry C* **2018**, *122*, 22460–22468.
- (23) Wu, L.; Hu, S.; Yu, W.; Shen, S.; Li, T. Stabilizing mechanism of single-atom catalysts on a defective carbon surface. *npj Computational Materials* **2020**, *6*, 23.
- (24) Akri, M.; Zhao, S.; Li, X.; Zang, K.; Lee, A. F.; Isaacs, M. A.; Xi, W.; Gangarajula, Y.; Luo, J.; et. al. Atomically dispersed nickel as coke-resistant active sites for methane dry reforming. *Nature Communications* **2019**, *10*, 5181.
- (25) Montini, T.; Melchionna, M.; Monai, M.; Fornasiero, P. Fundamentals and Catalytic Applications of CeO₂-Based Materials. *Chemical Reviews* **2016**, *116*, 5987–6041.
- (26) Senftle, T. P.; Van Duin, A. C.; Janik, M. J. Methane activation at the Pd/CeO₂ interface. *Acs Catalysis* **2017**, *7*, 327–332.
- (27) Lustemberg, P. G.; Ramírez, P. J.; Liu, Z.; Gutiérrez, R. A.; Grinter, D. G.; Carrasco, J.; Senanayake, S. D.; Rodriguez, J. A.; Ganduglia-Pirovano, M. V. Room-Temperature Activation of Methane and Dry Re-forming with CO₂ on Ni-CeO₂(111) Surfaces: Effect of Ce³⁺ Sites and Metal-Support Interactions on C–H Bond Cleavage. *ACS Catalysis* **2016**, *6*, 8184–8191.
- (28) Lustemberg, P. G.; Mao, Z.; Salcedo, A.; Irigoyen, B.; Ganduglia-Pirovano, M. V.; Campbell, C. T. Nature of the Active Sites on Ni/CeO₂ Catalysts for Methane Conversions. *ACS Catalysis* **2021**, *11*, 10604–10613.
- (29) Wang, J.; Gong, X.-Q. A DFT+U study of V, Cr and Mn doped CeO₂(111). *Applied Surface Science* **2018**, *428*, 377–384.
- (30) Mao, Q.; van Duin, A. C.; Luo, K. Investigation of methane oxidation by palladium-based catalyst via ReaxFF Molecular Dynamics simulation. *Proceedings of the Combustion Institute* **2017**, *36*, 4339–4346.

- (31) Hicks, R. F.; Qi, H.; Young, M. L.; Lee, R. G. Structure sensitivity of methane oxidation over platinum and palladium. *Journal of Catalysis* **1990**, *122*, 280–294.
- (32) Shi, S.; Han, Y.; Zang, Y.; Wang, Z.; Li, Y.; Zhang, H.; Liu, Z. Identification of Active Phase for Complete Oxidation of Methane on Palladium Surface. *2024*, *67*, 874–879.
- (33) Datye, A. K.; Bravo, J.; Nelson, T. R.; Atanasova, P.; Lyubovsky, M.; Pfefferle, L. Catalyst microstructure and methane oxidation reactivity during the Pd-PdO transformation on alumina supports. *Applied Catalysis A: General* **2000**, *198*, 179–196.
- (34) Chin, Y.-H. C.; Buda, C.; Neurock, M.; Iglesia, E. Consequences of Metal–Oxide Interconversion for C–H Bond Activation during CH₄ Reactions on Pd Catalysts. *Journal of the American Chemical Society* **2013**, *135*, 15425–15442.
- (35) Chen, B.; Lin, J.; Chen, X.; Chen, Y.; Xu, Y.; Wang, Z.; Zhang, W.; Zheng, Y. Cooperative Catalysis of Methane Oxidation through Modulating the Stabilization of PdO and Electronic Properties over Ti-Doped Alumina-Supported Palladium Catalysts. *ACS Omega* **2019**, *4*, 18582–18592.
- (36) Wang, J.; Wang, G.-C. Dynamic Evolution of Methane Oxidation on Pd-Based Catalysts: A Reactive Force Field Molecular Dynamics Study. *The Journal of Physical Chemistry C* **2022**, *126*, 14201–14210.
- (37) Du, J.; Zhao, D.; Wang, C.; Zhao, Y.; Li, H.; Luo, Y. Size effects of Pd nanoparticles supported over CeZrPAl for methane oxidation. *Catal. Sci. Technol.* **2020**, *10*, 7875–7882.
- (38) Petrov, A. W.; Ferri, D.; Krumeich, F.; Nachtegaal, M.; van Bokhoven, J. A.; Kröcher, O. Stable complete methane oxidation over palladium based zeolite catalysts. *Nature Communications* **2018**, *9*, 2545.

- (39) Zhang, T. et al. Simultaneously activating molecular oxygen and surface lattice oxygen on Pt/TiO₂ for low-temperature CO oxidation. *Nature Communications* **2024**, *15*, 6827.
- (40) Bunting, R. J.; Cheng, X.; Thompson, J.; Hu, P. Amorphous Surface PdOX and Its Activity toward Methane Combustion. *ACS Catalysis* **2019**, *9*, 10317–10323.
- (41) Xiong, H.; Kunwar, D.; Jiang, D.; García-Vargas, C. E.; Li, H.; Du, C.; Canning, G.; Pereira-Hernandez, X. I.; et. al. Engineering catalyst supports to stabilize PdOx two-dimensional rafts for water-tolerant methane oxidation. *Nature Catalysis* **2021**, *4*, 830–839.
- (42) Yue, S.; Praveen, C. S.; Klyushin, A.; Fedorov, A.; Hashimoto, M.; Li, Q.; Jones, T.; Liu, P.; Yu, W.; Willinger, M.-G.; Huang, X. Redox dynamics and surface structures of an active palladium catalyst during methane oxidation. *Nature Communications* **2024**, *15*, 4678.
- (43) Hellman, A.; Resta, A.; Martin, N. M.; Gustafson, J.; Trinchero, A.; Carlsson, P.-A.; Balmes, O.; Felici, R.; van Rijn, R.; Frenken, J. W. M.; Andersen, J. N.; Lundgren, E.; Grönbeck, H. The Active Phase of Palladium during Methane Oxidation. *The Journal of Physical Chemistry Letters* **2012**, *3*, 678–682.
- (44) Stotz, H.; Maier, L.; Boubnov, A.; Gremminger, A.; Grunwaldt, J.-D.; Deutschmann, O. Surface reaction kinetics of methane oxidation over PdO. *Journal of Catalysis* **2019**, *370*, 152–175.
- (45) Moncada Quintero, C. W.; Ercolino, G.; Poozhikunnath, A.; Maric, R.; Specchia, S. Analysis of heat and mass transfer limitations for the combustion of methane emissions on PdO/Co₃O₄ coated on ceramic open cell foams. *Chemical Engineering Journal* **2021**, *405*, 126970.

- (46) Koo, W.-T.; Yu, S.; Choi, S.-J.; Jang, J.-S.; Cheong, J. Y.; Kim, I.-D. Nanoscale PdO Catalyst Functionalized Co₃O₄ Hollow Nanocages Using MOF Templates for Selective Detection of Acetone Molecules in Exhaled Breath. *ACS Applied Materials & Interfaces* **2017**, *9*, 8201–8210.
- (47) Dai, Y.; Pavan Kumar, V.; Zhu, C.; MacLachlan, M. J.; Smith, K. J.; Wolf, M. O. Mesoporous Silica-Supported Nanostructured PdO/CeO₂ Catalysts for Low-Temperature Methane Oxidation. *ACS Applied Materials & Interfaces* **2018**, *10*, 477–487.
- (48) Wang, C.; Xu, Y.; Xiong, L.; Li, X.; Chen, E.; Miao, T. J.; Zhang, Y., Tianyu Lan; Tang, J. Selective oxidation of methane to C₂+ products over Au-CeO₂ by photon-phonon co-driven catalysis. *Nature Communications* **2024**, *15*, 7535.
- (49) Chen, Y. et al. Dynamic structural evolution of MgO-supported palladium catalysts: from metal to metal oxide nanoparticles to surface then subsurface atomically dispersed cations. *Chem. Sci.* **2024**, *15*, 6454–6464.
- (50) Kim, Y. K.; Hwang, S.-H.; Jeong, S. M.; Son, K. Y.; Lim, S. K. Colorimetric hydrogen gas sensor based on PdO/metal oxides hybrid nanoparticles. *Talanta* **2018**, *188*, 356–364.
- (51) Mhlongo, G. H.; Motaung, D. E.; Cummings, F. R.; Swart, H. C.; Ray, S. S. A highly responsive NH₃ sensor based on Pd-loaded ZnO nanoparticles prepared via a chemical precipitation approach. *Scientific Reports* **2019**, *9*, 9881.
- (52) McCarty, J. G. Kinetics of PdO combustion catalysis. *Catalysis Today* **1995**, *26*, 283–293, Selected papers presented at the International Workshop on Catalytic Combustion.
- (53) Yu, X.; Genz, N. S.; Mendes, R. G.; Ye, X.; Meirer, F.; Nachtegaal, M.; Monai, M.; Weckhuysen, B. M. Anchoring PdOx clusters on defective alumina for improved catalytic methane oxidation. *Nature Communications* **2024**, *15*, 6494.

- (54) Zheng, Z.; Cao, H.; Meng, J.; Xiao, Y.; Ulstrup, J.; Zhang, J.; Zhao, F.; Engelbrekt, C.; Xiao, X. Synthesis and Structure of a Two-Dimensional Palladium Oxide Network on Reduced Graphene Oxide. *Nano Letters* **2022**, *22*, 4854–4860.
- (55) Wang, T.; Yu, B.; Mu, L.; Chen, Z.; Xiao, C.; Peng, S. How to Characterize Supported PdOx Catalysts by CO-FTIR Spectroscopy: Importance of Surface Reduction and Particle Size. *The Journal of Physical Chemistry C* **2024**, *128*, 15356–15366.
- (56) Jiang, D.; Khivantsev, K.; Wang, Y. Low-Temperature Methane Oxidation for Efficient Emission Control in Natural Gas Vehicles: Pd and Beyond. *ACS Catalysis* **2020**, *10*, 14304–14314.
- (57) Bossche, M. V. d.; Grönbeck, H. Methane Oxidation over PdO(101) Revealed by First-Principles Kinetic Modeling. *Journal of the American Chemical Society* **2015**, *137*, 12035–12044.
- (58) Kulkarni, S. R.; Lezcano, G.; Velisoju, V. K.; Realpe, N.; Castaño, P. Microkinetic Modeling to Decode Catalytic Reactions and Empower Catalytic Design. *ChemCatChem* **2024**, *16*, e202301720.
- (59) Motagamwala, A. H.; Dumesic, J. A. Microkinetic Modeling: A Tool for Rational Catalyst Design. *Chemical Reviews* **2021**, *121*, 1049–1076.
- (60) Keller, K.; Lott, P.; Stotz, H.; Maier, L.; Deutschmann, O. Microkinetic Modeling of the Oxidation of Methane Over PdO Catalysts—Towards a Better Understanding of the Water Inhibition Effect. *Catalysts* **2020**, *10*.
- (61) Gupta, S.; Tomar, S.; Choi, J. H.; Jeong, H.; Lee, S.-C.; Bhattacharjee, S. Controlling Moisture for Enhanced Ozone Decomposition: A Study of Water Effects on CeO₂ Surfaces and Catalytic Activity. *The Journal of Physical Chemistry C* **2024**, *128*, 5889–5899.

- (62) Colussi, S.; Fornasiero, P.; Trovarelli, A. Structure-activity relationship in Pd/CeO₂ methane oxidation catalysts. *Chinese Journal of Catalysis* **2020**, *41*, 938–950.
- (63) Hohenberg, P.; Kohn, W. Inhomogeneous Electron Gas. *Phys. Rev.* **1964**, *136*, B864–B871.
- (64) Kohn, W.; Sham, L. J. Self-Consistent Equations Including Exchange and Correlation Effects. *Phys. Rev.* **1965**, *140*, A1133–A1138.
- (65) Aouina, A.; Gatti, M.; Chen, S.; Zhang, S.; Reining, L. Accurate Kohn-Sham auxiliary system from the ground-state density of solids. *Phys. Rev. B* **2023**, *107*, 195123.
- (66) Kresse, G.; Furthmüller, J. Efficient iterative schemes for ab initio total-energy calculations using a plane-wave basis set. *Phys. Rev. B* **1996**, *54*, 11169–11186.
- (67) Kresse, G.; Joubert, D. From ultrasoft pseudopotentials to the projector augmented-wave method. *Phys. Rev. B* **1999**, *59*, 1758–1775.
- (68) Dudarev, S. L.; Botton, G. A.; Savrasov, S. Y.; Humphreys, C. J.; Sutton, A. P. Electron-energy-loss spectra and the structural stability of nickel oxide: An LSDA+U study. *Phys. Rev. B* **1998**, *57*, 1505–1509.
- (69) Grimme, S.; Antony, J.; Ehrlich, S.; Krieg, H. A consistent and accurate ab initio parametrization of density functional dispersion correction (DFT-D) for the 94 elements H-Pu. *The Journal of Chemical Physics* **2010**, *132*, 154104.
- (70) Sanville, E.; Kenny, S. D.; Smith, R.; Henkelman, G. Improved grid-based algorithm for Bader charge allocation. *Journal of Computational Chemistry* **2007**, *28*, 899–908.
- (71) Penschke, C.; Paier, J.; Sauer, J. Oligomeric Vanadium Oxide Species Supported on the CeO₂(111) Surface: Structure and Reactivity Studied by Density Functional Theory. *The Journal of Physical Chemistry C* **2013**, *117*, 5274–5285.

- (72) Lawler, R.; Cho, J.; Ham, H. C.; Ju, H.; Lee, S. W.; Kim, J. Y.; Il Choi, J.; Jang, S. S. CeO₂(111) Surface with Oxygen Vacancy for Radical Scavenging: A Density Functional Theory Approach. *The Journal of Physical Chemistry C* **2020**, *124*, 20950–20959.
- (73) Fan, J.; Li, C.; Zhao, J.; Shan, Y.; Xu, H. The Enhancement of Surface Reactivity on CeO₂ (111) Mediated by Subsurface Oxygen Vacancies. *The Journal of Physical Chemistry C* **2016**, *120*, 27917–27924.
- (74) Tomar, S.; Bhadaria, B. S.; Jeong, H.; Choi, J. H.; Lee, S.-C.; Bhattacharjee, S. Single-Atom Pd Catalyst on a CeO₂ (111) Surface for Methane Oxidation: Activation Barriers and Reaction Pathways. *The Journal of Physical Chemistry C* **2024**, *128*, 8580–8589.
- (75) Henkelman, G.; Jónsson, H. Improved tangent estimate in the nudged elastic band method for finding minimum energy paths and saddle points. *The Journal of Chemical Physics* **2000**, *113*, 9978–9985.
- (76) Filot, I. A. W.; vanSanten, R. A.; Hensen, E. J. M. The Optimally Performing Fischer–Tropsch Catalyst. *Angewandte Chemie International Edition* **2014**, *53*, 12746–12750.
- (77) McQuarrie, D. A.; D., S. J. *Molecular Thermodynamics*; University Science Books: California, 1999.
- (78) Atkins, J. K. P.; Paula, J. d. *Atkins Physical Chemistry*; Oxford University Press: Oxford, 2018.
- (79) Trinchero, A.; Hellman, A.; Grönbeck, H. Methane oxidation over Pd and Pt studied by DFT and kinetic modeling. *Surface Science* **2013**, *616*, 206–213.
- (80) Jiao, H.; Wang, G.-C. Dry Reforming of Methane on Ni/LaZrO₂ Catalyst under External Electric Fields: A Combined First-Principles and Microkinetic Modeling Study. *ACS Applied Materials & Interfaces* **2024**, *16*, 35166–35178.

- (81) Deng, J.; Song, W.; Jing, M.; Yu, T.; Zhao, Z.; Xu, C.; Liu, J. A DFT and microkinetic study of HCHO catalytic oxidation mechanism over Pd/Co₃O₄ catalysts: The effect of metal-oxide interface. *Catalysis Today* **2020**, *339*, 210–219.
- (82) Moraes, P. I. R.; Bittencourt, A. F. B.; Andriani, K. F.; Da Silva, J. L. F. Theoretical Insights into Methane Activation on Transition-Metal Single-Atom Catalysts Supported on the CeO₂(111) Surface. *The Journal of Physical Chemistry C* **2023**, *127*, 16357–16366.
- (83) Spezzati, G.; Su, Y.; Hofmann, J. P.; Benavidez, A. D.; DeLaRiva, A. T.; McCabe, J.; Datye, A. K.; Hensen, E. J. M. Atomically Dispersed Pd–O Species on CeO₂(111) as Highly Active Sites for Low-Temperature CO Oxidation. *ACS Catalysis* **2017**, *7*, 6887–6891.
- (84) Zhang, J.; Yang, Y.; Qin, F.; Hu, T.; Zhao, X.; Zhao, S.; Cao, Y.; Gao, Z.; Zhou, Z.; Liang, R.; Tan, C.; Qin, Y. Catalyzing Generation and Stabilization of Oxygen Vacancies on CeO_{2x} Nanorods by Pt Nanoclusters as Nanozymes for Catalytic Therapy. *Advanced Healthcare Materials* **2023**, *12*, 2302056.
- (85) Yu, S.; Cheng, X.; Wang, Y.; Xiao, B.; Xing, Y.; Ren, J.; Lu, Y.; Li, H.; Zhuang, C.; Chen, G. High activity and selectivity of single palladium atom for oxygen hydrogenation to H₂O₂. *Nature Communications* **2022**, *13*, 4737.
- (86) Ouyang, R.; Curtarolo, S.; Ahmetcik, E.; Scheffler, M.; Ghiringhelli, L. M. SISSO: A compressed-sensing method for identifying the best low-dimensional descriptor in an immensity of offered candidates. *Physical Review Materials* **2018**, *2*, 083802.
- (87) Bhattacharjee, S.; Yoo, S.; Waghmare, U. V.; Lee, S. NH₃ adsorption on PtM (Fe, Co, Ni) surfaces: Cooperating effects of charge transfer, magnetic ordering and lattice strain. *Chemical Physics Letters* **2016**, *648*, 166–169.

- (88) Ouyang, R.; Ahmetcik, E.; Carbogno, C.; Scheffler, M.; Ghiringhelli, L. M. Simultaneous learning of several materials properties from incomplete databases with multi-task SISSO. *Journal of Physics: Materials* **2019**, *2*, 024002.